Glycine-A bio-capping agent for the bioinspired synthesis of nano-zinc oxide photocatalyst

Parita Basnet[1] · Dhrubajyoti Samanta[1] · T. Inakhunbi Chanu[2] · Satadru Jha[3] · Somenath Chatterjee[1]

Abstract

Structural modification of nanoparticles (NPs) for application-specific study is timely. In the present investigation, an attempt has been made for the bioinspired synthesis of zinc oxide (ZnO) NPs possessing different morphologies using glycine as the bio-capping agent. A variation in the amount of glycine during low-temperature mediated solid-phase synthesis indicated that a higher ratio of glycine directed the ensemble of nanohexagons into nanobundles which further formed nano-flower buds- like morphology, while least concentration formed agglomerated NPs and moderate concentration of glycine was able to modify the NPs' structure into nanorods. On the other hand, the utilization of solution-phase synthesis methods, i.e. co-precipitation and hydrothermal, led to the formation of thinner and thicker ZnO nanosheets, respectively. In terms of crystal-line structure, not much difference was observed in the lattice parameters or the unit cell of the crystal, with approximately similar crystallite sizes. From Fourier transform infrared spectroscopy, the functionalization of glycine from both the amine and the carboxyl group was noted. Further, it was found that the morphology and photoluminescence emission spectra of the samples were inter-related, wherein higher the agglomeration of the particles, greater the intensity of the visible region defect band was observed. The as-synthesized ZnO-photocatalysts were then employed for the degradation of rhodamine B (RhB), a major effluent of the textile industry. The photocatalytic activity of the samples was found to depend upon the surface area, which in turn was related to the morphology and the magnitude of green emission defect states. About 99% RhB degradation was obtained with ZnO possessing nano-flower buds-like morphology within 60 min of sunlight irradiation. Additionally, the role of reactive oxidative species and the stability of this photocatalyst were investigated.

1 Introduction

For the past many years, organic stabilizing agents, such as oleic acid, thioglycerol, and so on [1–6] along with other polymers and surfactants, have been utilized in the synthesis of zinc oxide (ZnO) nanoparticles (NPs), which impart the material its stability and also function as a structure modifier [7–13]. In recent times, stabilization of NPs using bio-capping agents, such as amino acids [14, 15], plant extracts [8, 13, 16], and so on, have attracted substantial interest since such structures are bio-compatible and therefore may be employed for biological applications including DNA or drug delivery, imaging, cosmetics, and others [17, 18]. Thus, amino acids (building blocks of protein) may be deliberated as ideal bio-compatible stabilizing agents. Based on the characteristics of their side chains, amino acids are categorized into various groups, wherein, the physical properties of the side chains may act as an influence during the interaction of amino acid residues with other compounds. Sreevalsa et al. [19] reported the synthesis of L-histidine-capped ZnO nanocrystals possesing potential bio-imaging application with regard to the intense photoluminescence (PL) emission observed at wavelength of ~ 527 nm. Another study based on the biological application of amino acid capped ZnO nanostructures (NSs) has been put forth by Ramani et al. [20]. They utilized three different types of amino acids, namely, L-alanine, L-threonine, and L-glutamine for the capping purpose of ZnO NSs, which resulted in the formation of various morphologies of ZnO. These NSs were then tested

✉ Somenath Chatterjee
somenath@gmail.com; somenath.c@smit.smu.edu.in

[1] Centre for Material Science and Nanotechnology, Sikkim Manipal Institute of Technology, Sikkim Manipal University, Gangtok, Sikkim, India

[2] Department of Chemistry, Nar Bahadur Bhandari Degree College, Gangtok, Sikkim, India

[3] Department of Chemistry, Sikkim Manipal Institute of Technology, Sikkim Manipal University, Gangtok, Sikkim, India

for their efficacy as anti-microbial agents against *Escherichia coli*, *Staphylococcus aureus*, *Klebsiella pneumoniae*, and *Bacillus subtilis*. They concluded the synergistic effect of the respective amino acids adsorbed at the surface of ZnO NSs toward microbial inhibition. Likewise, several reports state the bio-compatible nature of NPs when bound with amino acids [14, 20–22]. Moreover, amino acids perform a dual function by acting as an agglomeration controller as well as a shape modifier when used as a binder during NPs synthesis [15]. Wu et al. [15] employed a facile and bioinspired method for ZnO NSs synthesis using histidine as the structure-directing and structure-assembling agent. On varying the ratio of histidine used in their study, they obtained various ZnO hierarchical architectures, such as prism- and flower-like structures, including hollow microspheres. Thus, structure controlled synthesis of ZnO NPs is possible by adjusting the molar ratio of the bio-capping agent used in the study. In this current work, the amino acid glycine has been used as the bio-capping agent [23, 24] for the synthesis of various NSs of ZnO. Glycine is a neutral amino acid, which becomes amphoteric in aqueous medium. Therefore, the co-ordination or the capping ability of this amino acid and its influence over the structural, morphological, and optical aspects of ZnO is an interesting field to investigate (such as the formation of nano-flower buds with increased glycine concentration and nanosheets with different synthetic method).

There are several known synthesis methods of ZnO NPs in Refs. 16 and 25. An important fact that has been deduced by comparing the various synthesis methods is that they may also influence the structural formulation of the NPs, provided all the other parameters remain constant [7]. Elahe et al. [26], compared ZnO NPs based on the method of synthesis, i.e. biosynthesis and chemical synthesis. In their investigation, they found that biosynthesized ZnO NPs exhibited spherical and flower-like structures while chemical synthesis formed irregular surface morphology with much larger size, as compared to the former. Hence, morphology as well as size tuning of the NPs may be achieved by employing different synthesis approaches. However, for a method to prove effective, not only the purity of the final product is important, but also the corresponding cost-effectiveness and eco-friendliness of the method opted. Thus, simple and economical methods of glycine capped ZnO NPs (gly@ZnO NPs) have been considered in this study. In order to compare the differences in morphology, size, optical and structural properties of the as-synthesized ZnO NPs, three different methods of synthesis were considered in this study, namely, room-temperature solid state, co-precipitation and hydrothermal methods. The results exhibited interesting photophysical and morphological outcome. The choice of these synthesis techniques was based on the simplicity, economical, eco-friendly, and time saving properties. Moreover,

a co-relation based on the photoluminescence (PL) (optical) and Field emission scanning electron microscopy (FESEM) (morphological) studies has also been executed.

The problem of water scarcity is accelerating day-by-day [27, 28]. The major causes attributing to this ever-rising water pollution include improperly treated organic wastes (such as drugs, dyes, and other chemicals), heavy metal ions, etc., in addition to the solid plastic wastes [29, 30]. Organic dyes [31] mostly dissipate from the textile industry [32]. They have a complex molecular structure and are highly stable under ambient condition. Dyes are toxic and known to be carcinogenic in nature [33, 34]. Therefore, proper treatment of dyes before disposal into water bodies and the removal of already disposed dyes from aquatic media are of utmost importance and should be immediately taken into consideration. In the current research, the issue of degrading an organic dye, rhodamine B (RhB), into simple, non-harmful inorganic compounds has been accounted using the as-synthesized gly@ZnO NPs through the method of photocatalysis under natural solar irradiation. It has been well established through previous studies that reactive oxidative species (ROS) are primarily responsible for the overall photocatalytic degradation phenomenon [35, 36]; therefore, herein, a study related to the role of various ROS has been carried out using complimentary radical scavengers. Additionally, the stability of the as-synthesized photocatalyst has also been tested by performing the reusability test.

2 Experimental section

2.1 Chemical specifications

The chemicals used in this study were of analytical grade, which includes zinc acetate dihydrate ($Zn(CH_3COO)_2 \cdot 2H_2O$; Lobachemie make; molecular weight (MW) 219.50 g/mol), sodium hydroxide (NaOH; Lobachemie make; MW 40 g/mol), glycine ($C_2H_5NO_2$; Merck made; MW 75.07 g/mol), *p*-benzoquinone ($C_6H_4O_2$; Lobachemie; MW 108.095 g/mol), tertiary butyl alcohol ($C_4H_{10}O$; Merck made; MW 74.12 g/mol), ethylene diamine tetra acetate ($C_{10}H_{16}N_2O_8$; Merck make; MW 292.24 g/mol), methanol (CH_3OH; Rankem make), and rhodamine B ($C_{28}H_{31}ClN_2O_3$; Lobachemie make; 479.02; absorbance maxima in water: 550–554 nm). Deionized (DI) water with resistivity: 18.5 MΩ cm was used for all analysis.

2.2 Characterization

Information related to the crystal structure of Gly@ZnO NPs was obtained through PAN Alytical Spectris technologies PW 3040/60 X-ray diffractometer with Cu Kα$_1$ radiation ($\lambda = 1.54056$ Å), working voltage of 40 kV, and current of

30 mA. The existence of bio-capping fragments on ZnO NPs' surface was confirmed by Fourier transform infrared spectroscopic (FTIR) spectrum obtained from IRAffinity-1S Shimadzu Fourier transform infrared spectrophotometer. Optical properties were studied using UV–visible (UV–Vis) absorption data performed on Shimadzu 1800 UV–Vis spectrophotometer and PL spectroscopy measured on Shimadzu Spectrofluorophotometer (RF-5301 PC) with excitation wavelength (λ_{exc}) of 325 nm. Nitrogen (N_2) adsorption–desorption measurements were performed using Quantachrome Instruments, Autosorb-IQ volumetric adsorption analyser at −200 °C. For measurement, the samples were de-gassed at 150 °C for 4 h in a degassing port of the adsorption apparatus. The determination of specific surface area of the samples was carried out employing the adsorption data points obtained at (P/P_0) between 0.4 and 1.0 using Brunauer–Emmett–Teller (BET) equation. The mean (average) pore diameter was estimated using Barrett–Joyner–Halenda (BJH) method. The electrochemical impedance spectra (EIS) were recorded by Electrochemical Analyzer CHI608E, wherein silver/silver chloride (Ag/AgCl) was used as the reference electrode, Platinum wire as the counter-electrode and a glassy carbon electrode (GCE) as the working electrode. The electrochemical experiments were performed under dark conditions at room temperature. EIS responses were acquired using a well-cleaned GCE modified with the respective gly@ZnO samples. 1 mM potassium ferricyanide ($K_3Fe(CN)_6$) in 0.1 M potassium chloride (KCl) was employed as the redox analyte. The polarization of the electrode was performed at 0.25 V against the frequency range of 1 Hz to 100 kHz.

$[Fe(CN)_6]^{3-/4-}$ couple was used as the redox probe following the work performed by Maruthupandy et al. [37]. High-resolution transmission electron microscopy (HRTEM) with LaB_6 source and voltage of 200 kV equipped with an energy dispersive X-ray spectroscopy (EDS) was used for the microstructural and elemental analysis, respectively. Lux-meter (MEXTECH; model no. LX-1010B) was used to measure the solar intensity [(intensity = 1080 × 100) lx for all the photocatalytic experiments]. Morphological information was obtained using JEOL FESEM, Model: 7610F.

2.3 Synthesis

Tuning the morphology, size, microstructure, and optical properties of NPs largely depend upon their methods of synthesis and the type of capping agents used [38–41]. The use of low-temperature, top-down, and solid-state method is a highly efficient technique of preparing ZnO NPs [7, 42, 43] since this method is environmentally benign, cost-effective (requires only a simple mortar-pestle) and utilizes a minimum temperature (although high-temperature solid-state methods have also been reported, in the present study a temperature of 100 °C was employed). For identifying the morphology and size-tuning based on different synthesis methods, two bottom-up solution-phase approaches of ZnO NPs synthesis were also employed, namely, co-precipitation and hydrothermal methods. Stability of the as-synthesized NPs is another concern since the high energy NPs tend to aggregate and form bulk particles. To address this issue, the use of a bio-capping agent, glycine, was considered in this work. Figure 1 represents the different synthetic strategies
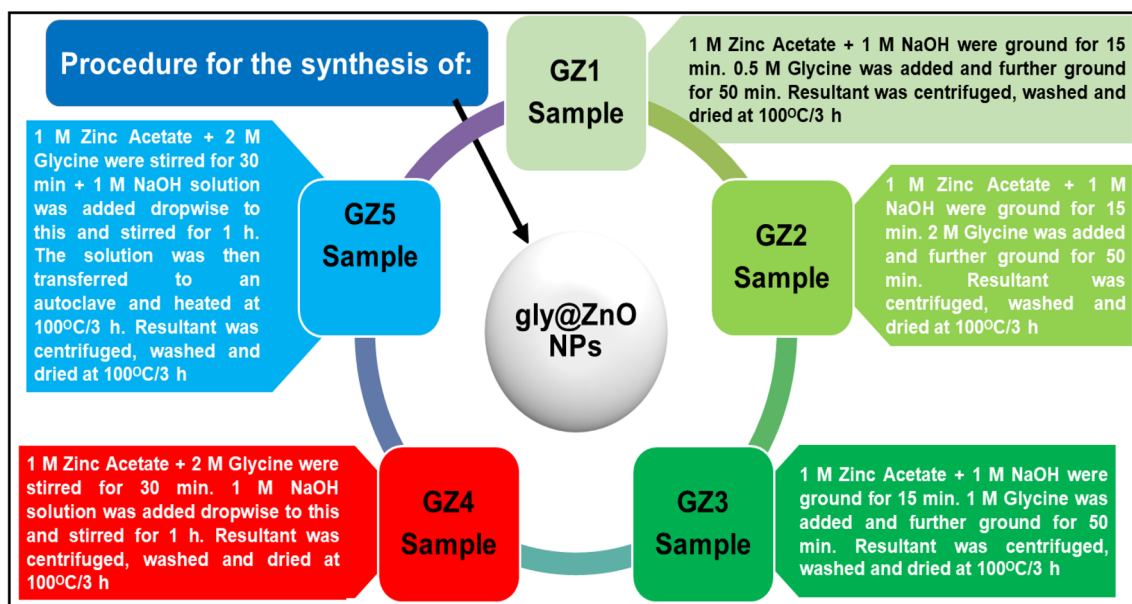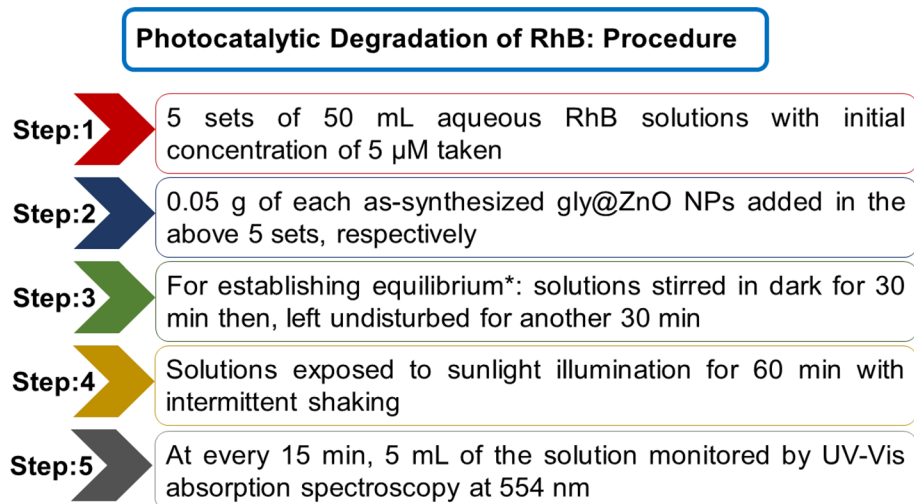

Procedure for the synthesis of:

GZ1 Sample: 1 M Zinc Acetate + 1 M NaOH were ground for 15 min. 0.5 M Glycine was added and further ground for 50 min. Resultant was centrifuged, washed and dried at 100°C/3 h

GZ2 Sample: 1 M Zinc Acetate + 1 M NaOH were ground for 15 min. 2 M Glycine was added and further ground for 50 min. Resultant was centrifuged, washed and dried at 100°C/3 h

GZ3 Sample: 1 M Zinc Acetate + 1 M NaOH were ground for 15 min. 1 M Glycine was added and further ground for 50 min. Resultant was centrifuged, washed and dried at 100°C/3 h

GZ4 Sample: 1 M Zinc Acetate + 2 M Glycine were stirred for 30 min. 1 M NaOH solution was added dropwise to this and stirred for 1 h. Resultant was centrifuged, washed and dried at 100°C/3 h

GZ5 Sample: 1 M Zinc Acetate + 2 M Glycine were stirred for 30 min + 1 M NaOH solution was added dropwise to this and stirred for 1 h. The solution was then transferred to an autoclave and heated at 100°C/3 h. Resultant was centrifuged, washed and dried at 100°C/3 h

gly@ZnO NPs

Fig. 1 Description of the procedures for synthesizing gly@ZnO NPs

**Fig. 2** Steps involved in the photocatalytic degradation studies of RhB by gly@ZnO NPs (*corresponds to [44])

Photocatalytic Degradation of RhB: Procedure

Step:1 5 sets of 50 mL aqueous RhB solutions with initial concentration of 5 µM taken

Step:2 0.05 g of each as-synthesized gly@ZnO NPs added in the above 5 sets, respectively

Step:3 For establishing equilibrium*: solutions stirred in dark for 30 min then, left undisturbed for another 30 min

Step:4 Solutions exposed to sunlight illumination for 60 min with intermittent shaking

Step:5 At every 15 min, 5 mL of the solution monitored by UV-Vis absorption spectroscopy at 554 nm

and the steps involved in the respective technique of gly@ZnO NPs formation. These samples have been designated as GZ1, GZ2, GZ3, GZ4, and GZ5 throughout the manuscript based on their synthesis method as given in Fig. 1. Further, the pH values of the samples measured during their synthesis were 12, 11.8, 11.9, 12.2, and 12.2 for GZ1, GZ2, GZ3, GZ4, and GZ5, respectively. However, during the washing process, these pH values were brought to the neutral level of ~ 7.

2.4 Photocatalytic activity measurements

The photocatalytic degradation of RhB was performed under solar irradiation with the average measured intensity of (1080×100) lx. Figure 2 represents the stepwise procedure employed for carrying out the photocatalytic degradation studies. Also, during the photocatalytic reaction, the 5 mL solution (aliquot) was subjected to UV–Vis spectral analysis, while the whole reaction mixture was covered with aluminium foil. After analysis, the aliquot was transferred back into the reaction medium and again exposed to sunlight irradiation. Degradation efficiencies of gly@ZnO NPs were calculated in percentage of decrease in the concentration of dyes relative to the absorption measurements. For the reusability test, GZ2 was chosen in three consecutive experiments while maintaining similar reaction conditions, i.e. 0.05 g GZ2 with 50 mL of RhB solution. The interval of exposure under solar radiation was also kept constant at 60 min. After each test, the photocatalyst was recovered through centrifugation and 50 mL of RhB solution was added. Rest of the steps were followed as before.
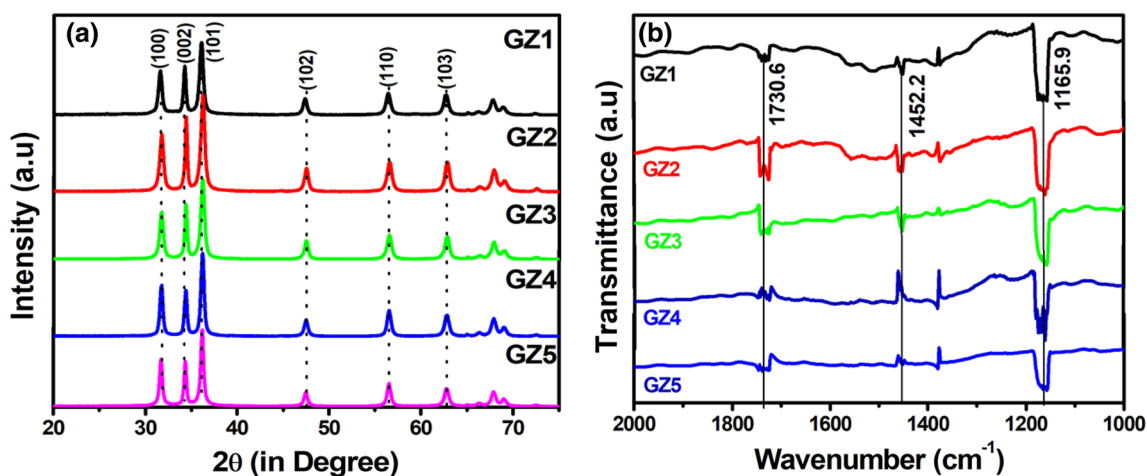
Fig. 3 a XRD spectra and **b** FTIR patterns of gly@ZnO NPs

Table 1 XRD data analysis corresponding to (101) crystal plane of gly@ZnO NPs

Sample	2θ	d-spacing (Å)	FWHM (°)	a (Å)	c (Å)	V (Å³)	Crystallite size (nm)
GZ1	36.145	2.4831	0.47222	3.257	5.234	48.08	18
GZ2	36.228	2.4775	0.49474	3.254	5.198	47.66	17
GZ3	36.228	2.4775	0.46207	3.251	5.209	47.67	19
GZ4	36.311	2.4721	0.38995	3.243	5.209	48.53	22
GZ5	36.228	2.4775	0.38203	3.251	5.209	47.67	22

3 Results and discussion

3.1 Characterization

3.1.1 Structural analysis

Figure 3a shows the XRD diffraction patterns of GZ1, GZ2, GZ3, GZ4, and GZ5 samples, respectively. In accordance with the JCPDS card no. for ZnO (36-1451) [7], the entire diffraction pattern corresponds to the ZnO hexagonal wurtzite structure. Additional peaks of $Zn(CH_3COO)_2$, sodium acetate, etc., or any other impurity peaks were not observed, which may be attributed to the high-purity formation of all gly@ZnO NPs. The consistency of 2θ values in case of all the samples indicates a negligible change in the ZnO lattice with insignificant microstrain effect. Employing the Debye Scherer equation [45], average crystallite sizes of gly@ZnO NPs were calculated in Table 1. Further, Table 1 provides information on the values of 2θ (peak positions), lattice constants (a and c), volume of unit cell (V), lattice (d) spacing, and full width at half maxima (FWHM) of (101) plane, respectively. From this table, it may be inferred that in case of all the samples, the lattice structure and unit cell do not exhibit a significant difference. Therefore, there is presumably no distortion in ZnO structure or changes in ZnO lattice. Additionally, not much variation in the average crystallite sizes of the as-synthesized gly@ZnO NPs may be noticed. The samples GZ1, GZ2, and GZ3 have approximately similar crystallite sizes, while GZ4 and GZ5 samples have slightly bigger crystallite sizes. This observation suggest that the structure-directing ability of glycine in the solid-state synthesis and solution-phase (i.e. co-precipitation and hydrothermal) techniques may have led to the formation of different microstructures as well as morphologies of gly@ZnO NPs.

The capping effect of glycine on the surface of gly@ZnO NPs was confirmed on the basis of FTIR spectra as shown in Fig. 3b, recorded in the scanning range of 600–2000 cm⁻¹. FTIR bands for free glycine are observed at 1596 cm⁻¹ for the antisymmetric vibrational mode of COO^- [$\nu_a(COO^-)$] and 1412 cm⁻¹ for the symmetrical vibrational mode of COO^- [$\nu_s(COO^-)$] [46]. In this work, shifts in the FTIR band positions were observed to 1730.61 and 1452.2 cm⁻¹,

respectively. These shifts may be ascribed to the symmetrical stretching vibrational mode of glycine indicating the coordination of the oxygen atom from the COO^- group [46]. The intensity of these peaks was observed to be the highest in case of GZ2, which may be attributed to the presence of more glycine moiety on ZnO surface. This validates the XRD analysis, wherein smaller crystallite size was observed for GZ2.

3.1.2 Morphological and elemental studies

The various properties, such as optical, surface, structural, and so on, of NPs depend greatly on the morphology of the as-formed particles [47, 48]. This means that the differences in the photophysical and catalytic properties of various samples may directly be co-related to the shape of the particles present in the respective samples. Different morphologies exhibit different surface area as well as varying degree of surface defects. Therefore, in order to fully understand and associate this fact with the present investigation, FESEM studies were performed, as provided in Fig. 4a–e. FESEM images of GZ1, GZ2, and GZ3 clearly point out the fact that the amount of capping material (glycine) during synthesis helps to regulate and modify the morphology of the NPs, which means, in this case, glycine acted as a structure-directing agent during the formation of ZnO NPs. When the amount of glycine was considered as least during synthesis (in GZ1), certain highly agglomerated structure with few ZnO nanorods was observed, as shown in Fig. 4a.

With increase in the amount of glycine to the most (in GZ2), it may be seen from Fig. 4b that 3–4 nanorods have agglomerated to form bundle-like structures which further agglomerated to ultimately form flower bud-like ZnO nanostructures. The uniformity of nanobuds in GZ2 may also be noted. In case of GZ3, the concentration of glycine was in-between that of GZ1 and GZ2, wherein ZnO nanorods arranged into bundles as shown in Fig. 4c. In this case, unlike GZ1, only agglomerated ZnO nanorods are seen, although these bundles have not inclined towards the formation of ZnO nanobuds as in the case of GZ2. Based on these results, the highest amount of glycine (as in the case of GZ2) was chosen for the synthesis of GZ4 and GZ5 but with two different synthesis approaches, so to understand
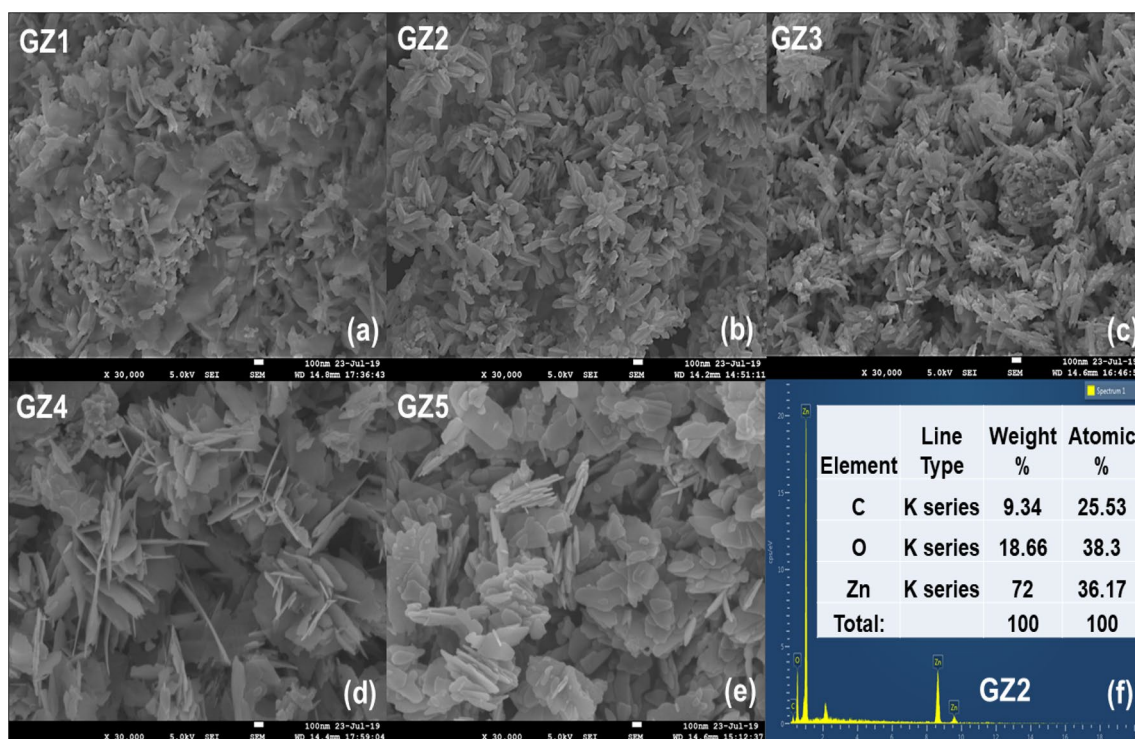
Fig. 4 FESEM images (100 nm scale bar) of **a** GZ1, **b** GZ2, **c** GZ3, **d** GZ4, **e** GZ5, and **f** elemental information of GZ2 as obtained through EDX spectroscopic measurements
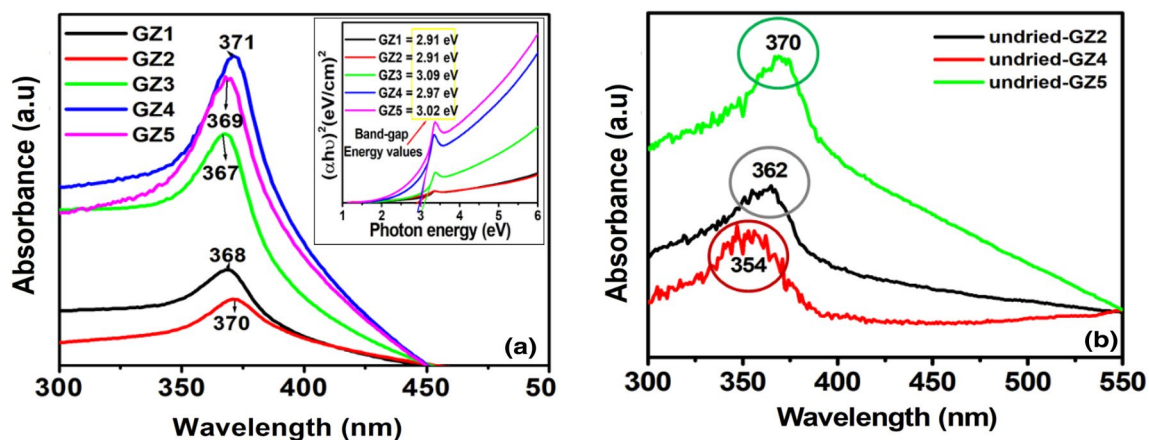
Fig. 5 a Absorbance spectra of gly@ZnO NPs with inset figure corresponding to the Tauc plots and **b** absorbance spectra of undried GZ2, GZ4 and GZ5

the role of the synthesis procedure in altering the morphology of ZnO NPs (for synthesis information, refer Sect. 2.3). Figure 4d illustrates sheet-like structures of GZ4 intertwined with one another, while in case of GZ5 (Fig. 4e), ZnO nanosheets with thicker surfaces are visible, including very few agglomerated rod-like structures. These changes in morphologies, as evidenced for GZ2, GZ4, and GZ5, owing to the utilization of different synthesis techniques, confirm

the role of various synthesis approaches for morphological tuning, when all the other experimental parameters are kept constant. In Sect. 3.2, the formation mechanism of these nanostructures of ZnO capped with glycine has been explained in detail. EDX analysis is an important tool to confirm the elemental composition of the sample. Figure 4f corresponds to the EDX spectra for GZ2, representing the presence of zinc, oxygen, and carbon in the sample. The

presence of carbon is attributed to the carbon grid used as a sample holder during analysis. The corresponding weight and atomic percentages of elements present in GZ2 are also shown, which are in accordance with the expected values.

3.1.3 Optical analysis

The gly@ZnO NPs were ultra-sonically dispersed in DI water and their UV–Vis absorbance recorded in the scanning range of 300–450 nm; the corresponding results are shown in Fig. 5a. The spectra were corrected for water contribution.

It may be observed that the representative absorption peaks of all the samples are slightly blue shifted with reference to the absorbance maximum of bulk ZnO (~ 380 nm). This ascertains the presence of smaller particles as compared to that in bulk ZnO [49, 50]. The narrow absorbance peaks may be accredited to the intrinsic band gap absorption of ZnO NPs arising from the electronic transitions, i.e. O_{2p} valence band (VB) → Zn_{3d} conduction band (CB) [51, 52]. The absorbance maxima of the samples are approximately at analogous positions which means that the particles have almost similar sizes. The inset of Fig. 5b depicts

the estimation of direct optical band gap energies (E_g) of the respective gly@ZnO samples, which were calculated employing Tauc equation [53]. The values of the band gap energies of gly@ZnO NPs (2.98 ± 0.07 eV) are lower than that of bulk ZnO (~ 3.3 eV) [54]. A reasonable justification to this observation may be the existence of various surface defects, such as valence-band donor level overlap of the surface states, defect levels within the band gap, and so on [55–57]. These defects may be identified through PL spectroscopic technique [58]. Further, in order to justify the formation of ZnO nuclei prior to heat treatment, the UV–Vis absorbance measurements of the undried GZ2, GZ4, and GZ5 were performed (similarly as before) which is shown in Fig. 5b. This graph clearly shows the absorbance peaks of ZnO with minor shifts in the peak positions relative to those of the corresponding dried gly@ZnO NPs. The probable reason for this observation may be the presence of zinc-hydroxyl groups, which are the ZnO growth species. It is well known that heat treatment increases the size of the particles via agglomeration [59, 60]; therefore, the hypsochromic shifts in the absorbance bands of undried samples as
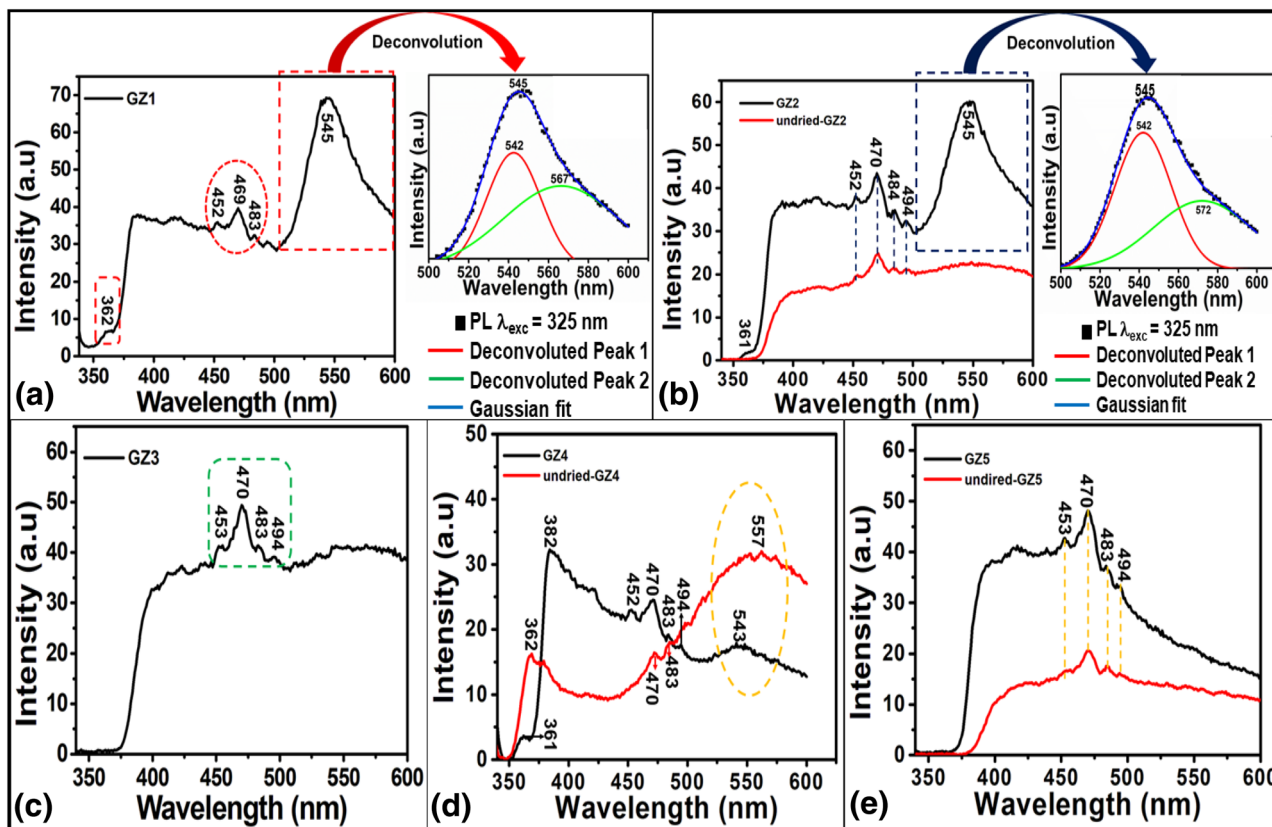
Fig. 6 PL spectra of **a** GZ1 with the inset figure depicting the deconvoluted spectra for the peak centred at 545 nm, **b** GZ2 and undried GZ2, with inset representing the deconvolution of the peak located at 545 nm of GZ2, **c** GZ3 and undried GZ3, **d** GZ4, **e** GZ5 and undried GZ5

compared to dried ones may be as a result of their comparatively larger size than undried gly@ZnO NPs.

PL studies were performed in the wavelength range of 340–600 nm. Figure 6 represents the PL spectra of all the as-synthesized gly@ZnO NPs. It is highly interesting to note that although most of the emission peaks are common in the as-synthesized samples (as shown in Fig. 6), the nature of green emission peak is similar for GZ1 and GZ2 and different for the rest, a broad green emission peak in GZ3 and GZ4 (both dried and undried), and no green emission in GZ5 (both dried and undried). This difference in the PL spectra may be co-related to their corresponding morphologies. The morphology of GZ1 depicts an agglomerated structure with few nanorods, while that of GZ2 is nanobundles, which have agglomerated into nanobuds-like structure. The agglomeration of individual particles is the highest in these two structures as compared to that in nanorods of GZ3 or nanosheets as in the case of GZ4 and GZ5. Therefore, agglomeration may have been the main reason for inducing green emission defect (of similar type) in these two samples. For comparison, PL was performed for GZ2, GZ4, and GZ5 samples before and after the heat treatment. In the PL spectra of undried GZ2, the green emission peak is broad and non-intense. This leads to the inference that in this sample, the heat treatment was basically the main factor which induced more defect states arising from green emission. In GZ4, although the PL spectra for dried and undried samples have the same nature, the intensity of the bands is opposite to each other, wherein up to blue-emitting region, the intensity is higher for dried sample and after that the intensity is relatively lower than that for undried GZ4, as observed in Fig. 6d. The nature of the PL spectra for both undried GZ5 and dried GZ5 is the same (Fig. 6e). Further, no green emission has been observed in this case, which leads to the conclusion that visible region-related defect states are not present in these samples. This means that the defect emission states corresponding to green emission are suppressed during the hydrothermal synthesis. The differences in intensity (as has been encountered in all the gly@ZnO NPs) may be attributed to the increase in the magnitude of the defect states pertaining to the visible region for the dried and undried samples.

Figure 6 displays the appearance of various emission peaks, which are explained as follows: (i) the near band-edge emission (NBE) (at 362 nm and 361 nm) for GZ1, GZ2 and GZ4, respectively, is due to exciton recombination; (ii) the blue emission band ranging from 450–495 nm is the characteristic band of ZnO, which may be attributed to the electron–hole pair recombination between singly ionized Zn interstitial state (I^*_{Zn}) and the valence band [61]; and (iii) the green emission bands appearing for GZ1, GZ2, and GZ4, respectively, may be ascribed to the recombination of electrons arising from the deep level isolated singly ionized oxygen centres with the photo-produced holes [61]. Therefore, it may be inferred that the PL spectra of the samples may be manipulated or controlled by tuning the morphology and phase structures.

3.1.4 Specific surface area analysis

In order to determine the specific surface area and the porous nature of the as-synthesized gly@ZnO NPs, N_2 adsorption–desorption isotherms and Barret–Joyner–Halenda (BJH) pore size distribution curves of GZ2, GZ3, and GZ4 were studied, respectively, and have been presented in Fig. 7a–c.

The obtained isotherms of these samples belong to type-IV N_2 adsorption–desorption isotherm with an H1 hysteresis loop at relative pressure (P/P_o) ranging from 0.4 to 1.0. The insets of Fig. 7a–c represent the corresponding curves of the BJH pore size distribution. The BJH pore size distribution of GZ2 and GZ5 reveals the mesoporous nature of these samples, while that of GZ4 exhibits its macroporous nature [62–64]. The average pore diameters of GZ2, GZ4, and GZ5 are given in Fig. 7d along with their BET-specific surface areas. The highest BET-specific surface area has been obtained for GZ2, which may be attributed to its 3D-flower bud-like morphology as obtained from FESEM image.

### 3.1.5 Electrochemical impedance spectral (EIS) analysis

The PL analyses of the samples provided an insight into the presence of defect states in the samples. These defects may strongly influence the electrical properties of the samples as well as their photocatalytic activities. In this regard, EIS analyses were performed since it is a powerful technique to probe into the electrical characteristics of the as-prepared ZnO semiconductor nanomaterials [65].

Figure 8 represents the Nyquist plots of all the gly@ZnO samples. As may be observed, there is only one semi-circle arc in the Nyquist plots of all the samples. These semi-circle arcs represent the recombination resistance, which in turn is related to the electronic recombination at the interface. Further, the radius of the arc signifies the recombination resistance [66, 67], whose value is inversely proportional to the values of the recombination rate and density of electrons in the material. In this case, the recombination resistance of GZ1 and GZ2 is relatively much higher as compared to other samples. Since larger recombination resistance corresponds to lower rates of recombination, comparatively greater electron transfer occurs in these samples. This explanation ultimately implies the higher rates of electron transfer in GZ1 and GZ2 as compared to other samples.
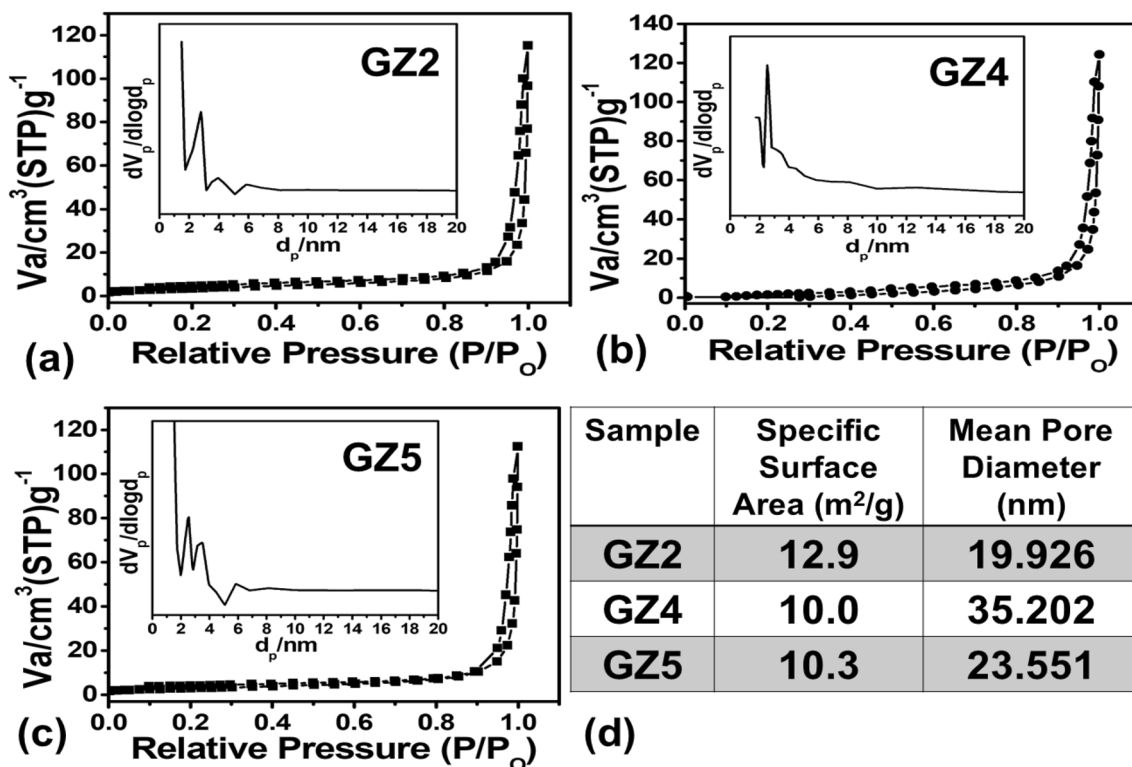
Fig. 7 a–c N_2 adsorption–desorption isotherm (BET) and BJH pore size distribution (inset) and **d** corresponding specific surface area and average pore diameters of GZ2, GZ4, and GZ5, respectively
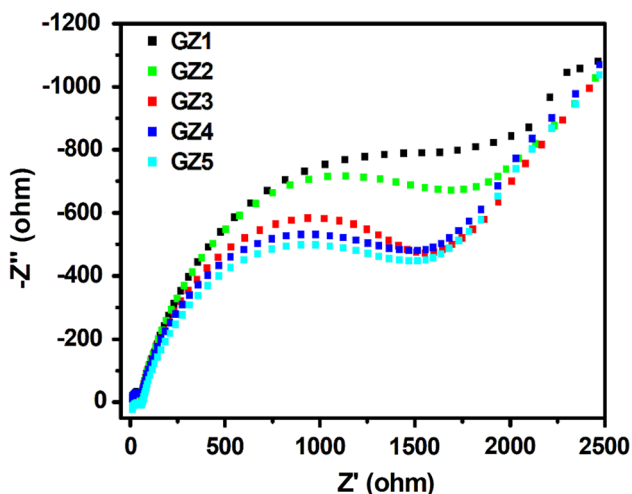
**Fig. 8** Electrical impedance spectra: Nyquist plot of gly@ZnO samples under dark conditions

3.1.6 Microstructural studies

To determine the microstructure of GZ2, HRTEM characterization was carried out as depicted in Fig. 9a–c, respectively. As may be observed from Fig. 9a, b, hexagonal particles are present in the microstructure of GZ2. This corresponds to the fact that hexagonal particles formed bundles, which later agglomerated to form a flower bud-like GZ2 nanostructures. The average length and breadth of the particles were calculated to be in the range of 10–12 nm and 25–30 nm, respectively. Figure 9c represents the HRTEM image of GZ2 sample. The value of *d*-spacing, as calculated from this image, was found to be 2.09 Å for (101) plane, which is consistent with the value as obtained from the XRD analysis (2.48 Å), as reported in Table 1. Figure 9d represents the selected area electron diffraction (SAED) pattern of GZ2 sample, which indicated the polycrystalline nature of the sample. For other samples also, similar crystalline nature was observed.

3.2 Formation mechanism of various morphologies of gly@ZnO NPs

Based on the aforementioned results, the probable formation mechanism of various morphologies of gly@ZnO NPs has been discussed in this section. It has been established that hydroxyl ions and amino acid molecules, in this case glycine molecule, act as competitive ligands toward Zn^{2+} owing to the various rates of formation constants of the complex [15, 68]. In case of GZ1 and GZ3, the ratio of glycine/Zn^{2+}/
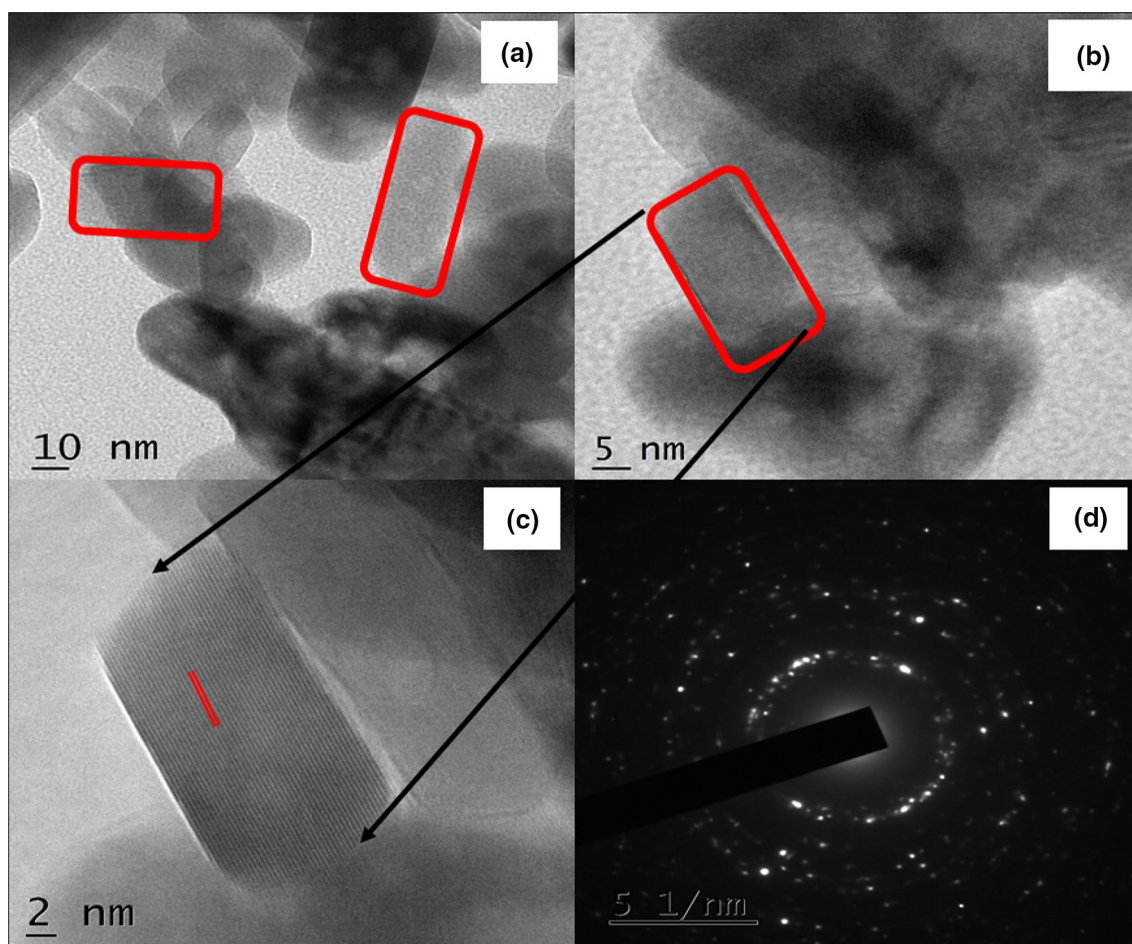
Fig. 9 TEM images of GZ2 at **a** magnification of 10 nm, **b** magnification of 5 nm, **c** HRTEM image displaying the lattice fringes, and **d** SAED pattern

NaOH was maintained at 0.5:1:5 and 1:1:5, respectively. Thus, OH⁻ must have played a vital role in directing the structure of the as-formed NPs. Since the concentration of glycine was much lesser than that of the hydroxide precursor, formation of $Zn(OH)_n$ complex may have been greater than $Zn(glycine)_n$ complex, and this must have been the reason for the formation of rod-like nanostructures, wherein elongation of the c-axis was predominant [7]. It is also to be noted that in case of GZ1, the amount of glycine was insufficient in exhibiting its potential capping application, whereas in case of GZ3, as the amount of glycine was doubled, agglomeration-controlled synthesis of ZnO NPs was observed with the overall conversion of particles into rod-like structures. In case of GZ2, the ratio of the precursors used was 2:1:5. This increased concentration of glycine led to its adsorption on the surface of ZnO nuclei (analogous to FTIR result) and as a consequence, nanobuds-like structure resulted from the agglomeration of nanobundles. It is evident from the structures of GZ4 and GZ5 that unlike in the previous cases,

herein, the formation of nanosheets has taken place. The most important distinction between GZ1, GZ2, GZ3, GZ4, and GZ5 is their method of synthesis, respectively.

The former were prepared through the grinding process in the solid-state phase, while the latter were prepared via solution-based systems. Further, the contact time of the reacting molecules was longer in the latter as compared to the former. Through this discussion, it may be concluded that the solution-based synthesis methods favour the formation of nanosheets when glycine is used as a capping agent under parameters as described in Fig. 1. The mechanism of nanosheets formation (GZ4) may be explained as the mixing of the precursors led to the formation of ZnO nuclei, which then grew into nanoclusters. Further, ZnO growth species, i.e. $Zn(OH)_n$, favourably adsorbed onto the surface of ZnO nuclei and consequently, assisted the growth along c-axis in order to reduce the energy otherwise required for hexagonal crystal structure [69–71]. Thereafter, ZnO NPs underwent oriented coalescence leading to the formation

Fig. 10 Pictorial representation of gly@ZnO NPs formation mechanism
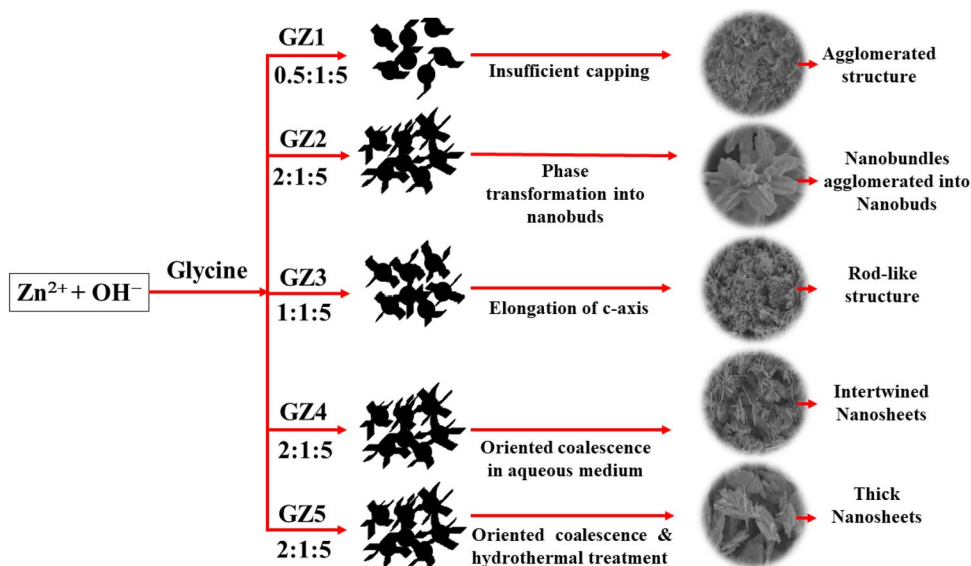
of nanosheets-like structure. The formation of thicker nanosheets, as in the case of GZ5, relies on the defect states available in nanosheets (as in GZ4). Since the synthesis procedures of GZ4 and GZ5 are similar up to the stirring step

after the mixing of precursors, it may be assumed that during this time interval, thinner nanosheets as in GZ4 were already formed. The defects available in these nanosheets must have acted as nucleation sites during the hydrothermal process
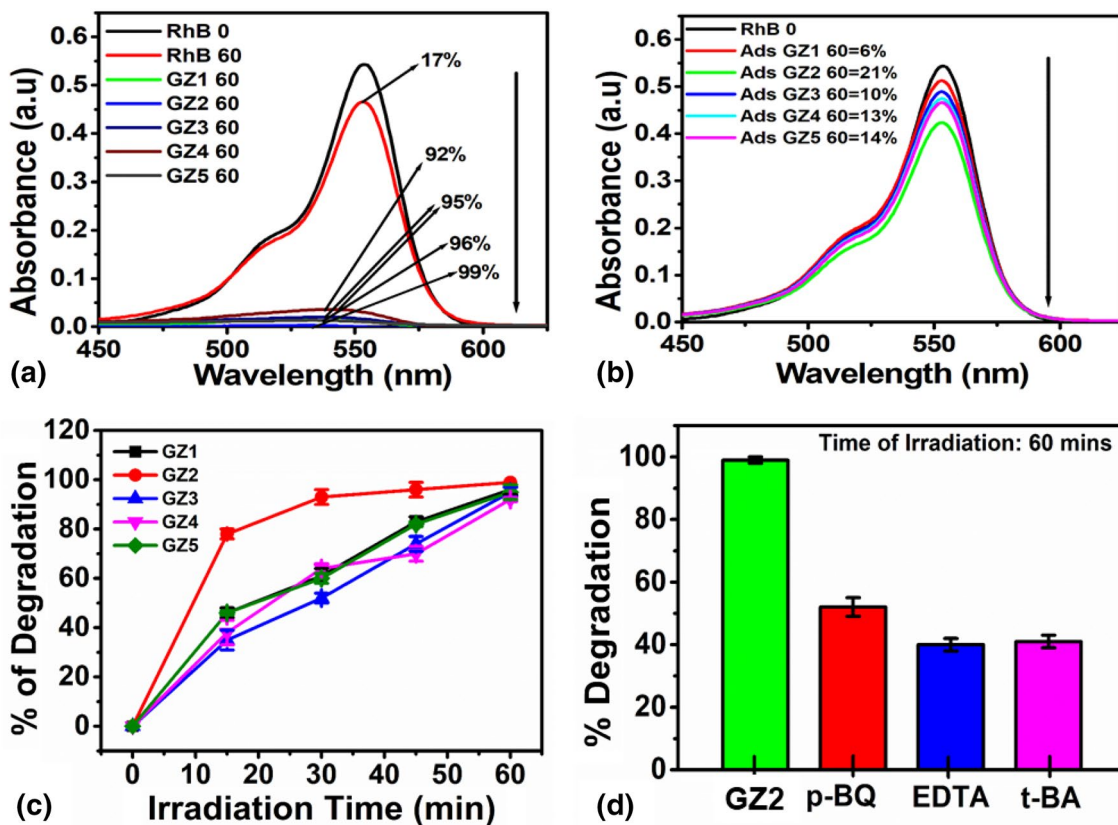
Fig. 11 **a** UV–Vis absorbance spectra illustrating decrease in the absorbance maxima of RhB with time of sunlight irradiation, **b** adsorption spectra (under dark condition) of RhB by gly@ZnO samples, **c** percentage of photocatalytic degradation of RhB by gly@ZnO samples, and **d** radical scavenging experiment depicting the role of ROS in the photocatalytic degradation process by GZ2

that the growth of secondary nanosheets occurred [71] and thereby resulted in the formation of thicker nanosheets. A schematic has been presented in Fig. 10 to pictorially describe these explanations.

3.3 Application: rhodamine B degradation studies

The toxicity of RhB for marine as well as terrestrial species has been previously discussed in Refs. 72–74. Pertaining to the fatal effects of this harmful dye, the present investigation has attempted to degrade the complex molecular structure of the RhB organic dye into simple, non-harmful inorganic compounds.

The UV–Vis absorption maximum of this dye in aqueous medium is at 554 nm due to the $n \rightarrow \pi*$ transition from C=N, C=O groups present in the dye structure [75]. The decrease in this absorbance maximum was used to estimate the decolourization level.

Figure 11a represents the ongoing temporal absorption of RhB solution during natural solar irradiation by the respective gly@ZnO samples. Photolysis of RhB solution was also conducted under identical conditions for comparison. It may be observed that negligible reduction of ~ 17% in the absorbance maximum of RhB solution occurred upon photolysis, indicating the stability of RhB under sunlight illumination. Upon addition of the respective gly@ZnO samples (procedure given in Sect. 2.4), sharp decrease in the absorbance corresponding to > 90% was noticed. After 60 min of experimentation, the bright pink colour of RhB solution completely vanished and turned colourless. This decrease in the absorbance peak to minimum (~ 0) may be attributed to the breakdown of both the chromophoric group and the dye dimer of RhB [7]. Therefore, enhanced acceleration in the degradation process was possible due to the presence of the photocatalysts (i.e. gly@ZnO NPs). Further, the decomposition of RhB takes place via two mechanisms, i.e. (i) the destruction of conjugated structure and (ii) *N*-de-ethylation [76–78]. This means that RhB may directly break down to its photo-degraded end products like CO_2, NO_3 or NO_x or through the stepwise *N*-de-ethylation process, respectively. The dominance of *N*-de-ethylation may be specified by a blue shift in the absorbance maxima of RhB accompanied by its decrease in intensity. As is clear from Fig. 11a, no blue shift in the peak at 554 nm was observed upon degradation. Therefore, in this case, the photocatalytic degradation of RhB was pre-dominated by the process of conjugated structure breakdown.

Figure 11b represents the adsorption spectra after 60 min of mixing RhB solution with the respective gly@ZnO samples under dark conditions. It may be observed from this graph that the maximum adsorption efficiency was 21% exhibited by GZ2 as compared to other samples. Also, from Fig. 11a, the degradation percentage of photolysis was only 17%. These results signify that both photocatalyst and photons are imperative for the complete removal of RhB dye from aqueous medium. Further, when the RhB and GZ2 reaction mixture was directly exposed to sunlight, without performing the adsorption experiment, a relatively lower photocatalytic degradation efficiency was acquired (~ 15%) than that obtained following the adsorption studies. This experiment, therefore, proves the synergistic role of adsorption and photodegradation mechanisms for the removal of RhB dye from aqueous medium. Figure 11c shows the percentage of RhB degradation with respect to specific time of irradiation. It may be noticed that under 15 min of natural solar irradiation, ~ 80% of RhB solution was degraded by GZ2, while the other samples degraded less than ~ 50%. This analysis indicates the highly proficient photodegradation property of GZ2 as compared to other samples under study. The activity of reactive oxidative species (ROS) in the reaction medium, particularly, hydroxyl radicals (OH·), superoxide radicals ($O_2^{·-}$) and holes (h^+), is responsible for the photocatalytic degradation process. These ROS undergo redox reactions with the dye molecules adsorbed at the surface of the photocatalyst and form the degradation products like carbon dioxide (CO_2), water (H_2O) and simple inorganic compounds [44]. In this work, due to the higher degradation efficiency of GZ2 towards RhB, the radical scavenging experiment was performed in case of GZ2 and the results are depicted in Fig. 11d. The radical scavengers used were 15 mM t-BA for ·OH, 15 mM *p*-BQ for $O_2^{·-}$ and 15 mM EDTA for trapping h^+. Maximum degradation occurred in the absence of any quenching agent while the percentage of degradation quickly reduced upon their addition. This result indicates that all ROS are important for efficient photocatalytic degradation of RhB. On the other hand, minimum degradations were observed with EDTA and t-BA, indicating that the complimentary radicals, namely, h^+ and OH·, respectively, were contributing more toward the photocatalytic degradation mechanism of RhB as compared to $O_2^{·-}$.

The photocatalytic activity of the as-prepared gly@ZnO NPs was studied more precisely based on their RhB degradation kinetics. The linear fitting of natural logarithm for the concentration of RhB at different irradiation time fitted well by an exponential decay curve signifying pseudo-first-order kinetics as shown in Fig. 12a. The corresponding rate constant (*k*) values were calculated using Eq. 1 given below

$$\ln \frac{C_t}{C_0} = -kt \tag{1}$$

where C_0 and C_t are the initial and final RhB concentrations at time *t* and *k* is the pseudo-first-order rate constant.

The calculated values of rate constants for the photocatalytic degradation of RhB by the as-prepared gly@ZnO NPs
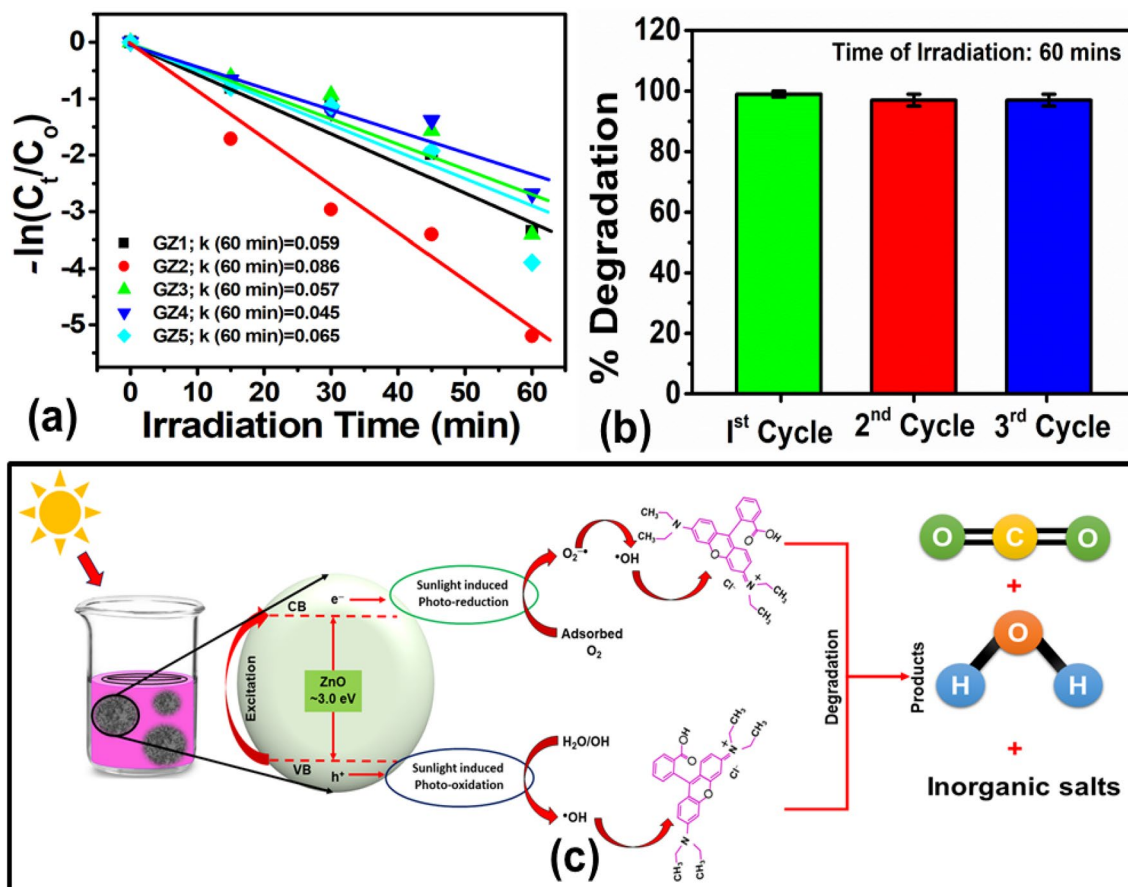
Fig. 12 **a** Kinetics of photocatalytic RhB degradation by gly@ZnO NPs, **b** reusability test of GZ2 against three consecutive cycles, and **c** schematic representation of the degradation mechanism

Table 2 Rate constant values of gly@ZnO NPs for RhB degradation and their corresponding degradation percentages

S. no.	Sample	Rate constant (k) in min^{-1}	% of RhB degradation
1	GZ1	0.059	92
2	GZ2	0.089	99
3	GZ3	0.057	95
4	GZ4	0.045	96
5	GZ5	0.065	95

are given in Table 2 along with their corresponding degradation percentages. It is evident from Table 2 that the sample GZ2 has the highest value of the rate constant indicating the highest photocatalytic degradation efficiency amongst the other gly@ZnO NPs. Further, photostability of the catalyst is of paramount importance to carry out a low-cost process. In this regard, the reusability test of GZ2 was performed over three successive cycles, depicted in Fig. 12b. It was observed that negligible change in the degradation efficiencies was

observed, indicating the stability of GZ2 sample. Hence, GZ2 may prove to act as an industrially viable photocatalyst.

The reason for the higher photocatalytic degradation efficiency of GZ2 as compared to other samples may be attributed to relatively higher surface area of GZ2 due to morphology as well as greater magnitude of visible light defect states. It has been reported in literature that the 3-D flower-like morphology has more surface area as compared to 2-D nanorods or nanosheets [79]. In this study also, a similar trend was observed, wherein the ZnO with 3D nano-flower bud-like morphology exhibited a higher specific surface area as compared to those with 2D nanosheets-like morphology, as confirmed through N_2 adsorption–desorption analysis. As was observed through PL studies, the intensity of visible light defect emission was the highest in case of GZ2. It has been well established that the higher magnitude of defect states increase the lifetime of electron or hole as well as the effective surface area of the particles. This higher recombination resistance of GZ2 was recognized through EIS analysis. Therefore, greater adsorption of the dye by GZ2 was possible through increased surface area, while higher rates of electron transfer accelerated the photodegradation of RhB

Table 3 Comparison of photocatalytic dye degradation efficiencies of ZnO nanostructures synthesized using different capping agents

Photocatalysts	Capping agents	Pollutants (model dyes)	Energy source	Degradation (%)	Refs.
ZnO	EDTA	Malachite Green	Sunlight	94.14	[80]
	Citric acid			80.15	
	Oleic acid			67.65	
ZnO	Oxalic acid	Methyl Orange (MO)	UV irradiation	99.70	[81]
		Congo Red		99.21	
		Direct Black-38		99.45	
ZnO	–	Methylene Blue (MB)	Blacklight irradiation	94	[82]
		Reactive Orange		91	
ZnO	Glucose	MO	UV lamp	Complete degradation	[83]
ZnO	Succinic acid (fuel)	MB	UV light	88	[84]
			Sunlight	94	
Porous silica supported ZnO and unsupported ZnO	HMTA	MB	UV light	71.7 and 48.2	[85]
La–ZnO	–	MB	UV light	78	[86]
Sm–ZnO				84	
Dy–ZnO				91	
Nd–ZnO				98	
ZnO				52.4	
Fe/Cd–ZnO	Citric acid	MB	Visible light	82	[87]
ZnO		RhB		76	
Mn–ZnO	Oxalic acid	Direct Blue 15	UV light	74 by Ag–ZnO	[88]
Ag–ZnO			Visible light	70 by Cu–ZnO	
Cu–ZnO					
Mn–ZnO					
ZnO					
Nd–ZnO	–	Rhodamine 6G	UV light	97.39	[89]
ZnO				65.51	
ZnO	Glycine	RhB	Solar irradiation	99	This study

molecules by GZ2. Since the defect states increases the lifetime of electron or hole as well as the effective surface area of the particles, greater adsorption and thereby degradation of RhB molecules were possible with this sample.

The possible mechanism during the interaction of photons with dye molecules and photocatalyst has been reported elsewhere by the Authors for other samples [7, 13, 16] and is schematically presented in Fig. 12c for the present study. The probable products of degraded RhB molecules, as mentioned in this figure, are based on previous studies [62, 90]. Table 3 represents the comparison between the photocatalytic dye degradation efficiencies of ZnO nanostructures as collected from previous literature with the current study. It may be seen from this table that the current work is amongst the samples exhibiting the highest degradation efficiencies.

4 Conclusions

In this study, glycine was used as a structure modifier and an agglomeration controller of the as-synthesized particles. Three different methods of synthesis were compared on the basis of their properties and photocatalytic performance, i.e. solid state, co-precipitation, and hydrothermal methods. Based on the overall results, the following conclusions have been drawn:

1 In solid-state synthesis, the amount of glycine determined the structural orientations of the particles, as was observed from GZ1, GZ2, and GZ3 samples. With an increase in the glycine amount, the agglomerated particles first orientated into rod-like structures, while further increase led to the arrangement of these rods into flower-like morphology. These results confirmed the requirement for the optimum usage of capping agent for structural modification of the NPs.

2. On changing the synthetic process to solution phase, the formation of nanosheet-like structures occurred. This result clearly proves the alteration in the physical form of the NPs upon the utilization of varying synthetic processes.

3. After analysing the PL data of all the samples, it was observed that the nature of the PL curve was strongly co-related to the morphology of the as-synthesized ZnO NPs.

4. Further, higher magnitude of visible region defect levels corresponded to the effective surface area of the as-synthesized particles and consequently resulted in higher photocatalytic activity.

5. The optical band gap energy was found to exhibit hypsochromic shift as compared to that of bulk ZnO due to the presence of various defect states in the samples.

6. The specific surface area of gly@ZnO NPs greatly dependent upon their morphology, wherein nano-flower buds-like ZnO exhibited the highest surface area as compared to other structures which may be attributed to its 3D structure and higher magnitude of surface defects.

7. Through EIS analyses of all the samples, the greater recombination retardation was observed in case of GZ1 and GZ2 samples, indicating the relatively higher electron transfer in these samples amongst others.

8. RhB degradation was observed to be relatively maximum in case of GZ2 owing to its 3D flower bud-like structure possessing comparatively higher surface area due to a greater magnitude of the defect states as well as lower recombination rates corresponding to higher electron transfer.

9. GZ2 exhibited excellent stability as a photocatalyst making it a potential candidate for industrial usage.

Therefore, the morphology and the corresponding properties of the NPs may be tuned employing different synthetic processes.

Compliance with ethical standards

Conflicts of interest The authors declare that they have no conflict of interest.

References

1. R. Tripathi, A. Kumar, C. Bharti, T.P. Sinha, Dielectric relaxation of ZnO nanostructure synthesized by soft chemical method. Curr. Appl. Phys. **10**, 676–681 (2010). https://doi.org/10.1016/j.cap.2009.08.015

2. S.S. Ashtaputre, A. Deshpande, S. Marathe, M.E. Wankhede, J. Chimanpure, R. Pasricha, J. Urban, S.K. Haram, S.W. Gosavi, S.K. Kulkarni, Synthesis and analysis of ZnO and CdSe nanoparticles. Pramana J. Phys. **65**, 615–620 (2005). https://doi.org/10.1007/bf03010449

3. L. Wu, Y. Zhang, G. Yang, S. Zhang, L. Yu, P. Zhang, Tribological properties of oleic acid-modified zinc oxide nanoparticles as the lubricant additive in poly-alpha olefin and diisooctyl sebacate base oils. RSC Adv. **6**, 69836–69844 (2016). https://doi.org/10.1039/c6ra10042b

4. M.A. Morris, L. Chen, J.D. Holmes, S. Ramrez-Garca, Facile synthesis of monodisperse ZnO nanocrystals by direct liquid phase precipitation. J. Nanomater. (2011). https://doi.org/10.1155/2011/853832

5. P.D. Cozzoli, A. Kornowski, H. Weller, Colloidal synthesis of organic-capped ZnO nanocrystals via a sequential reduction–oxidation reaction. J. Phys. Chem. B. **109**, 2638–2644 (2005). https://doi.org/10.1021/jp0457139

6. A.K. Singh, V. Viswanath, V.C. Janu, Synthesis, effect of capping agents, structural, optical and photoluminescence properties of ZnO nanoparticles. J. Lumin. **129**, 874–878 (2009). https://doi.org/10.1016/j.jlumin.2009.03.027

7. P. Basnet, D. Samanta, T. Inakhunbi Chanu, J. Mukherjee, S. Chatterjee, Assessment of synthesis approaches for tuning the photocatalytic property of ZnO nanoparticles. SN Appl. Sci. **1**, 633 (2019). https://doi.org/10.1007/s42452-019-0642-x

8. P. Basnet, T.I. Chanu, D. Samanta, S. Chatterjee, J. Mukherjee, Removal of cationic water pollutants using PEG stabilized ZnO nanoparticles under solar irradiation. in Proceedings of the Dae Solid State Physics Symposium 2018 (2019), p. 030204. https://doi.org/10.1063/1.5113043

9. X. Sun, X. Chen, Z. Deng, Y. Li, A CTAB-assisted hydrothermal orientation growth of ZnO nanorods. Mater. Chem. Phys. **78**, 99–104 (2003). https://doi.org/10.1016/S0254-0584(02)00310-3

10. H. Zhang, D. Yang, Y. Ji, X. Ma, J. Xu, D. Que, Low temperature synthesis of flowerlike ZnO nanostructures by cetyltrimethylammonium bromide-assisted hydrothermal process. J. Phys. Chem. B. **108**, 3955–3958 (2004). https://doi.org/10.1021/jp036826f

11. T.T. Trinh, K.-Q. Tran, X.-Q. Zhang, R.A. van Santen, E.J. Meijer, The role of a structure directing agent tetramethylammonium template in the initial steps of silicate oligomerization in aqueous solution. Phys. Chem. Chem. Phys. **17**, 21810–21818 (2015). https://doi.org/10.1039/C5CP02068A

12. J.Q. Hu, Q. Li, N.B. Wong, C.S. Lee, S.T. Lee, Synthesis of uniform hexagonal prismatic ZnO whiskers. Chem. Mater. **14**, 1216–1219 (2002). https://doi.org/10.1021/cm0107326

13. P. Basnet, D. Samanta, T.I. Chanu, J. Mukherjee, S. Chatterjee, Tea-phytochemicals functionalized Ag modified ZnO nanocomposites for visible light driven photocatalytic removal of organic water pollutants. Mater. Res. Express. **6**, 085095 (2019). https://doi.org/10.1088/2053-1591/ab234e

14. J. Zhou, N.S. Xu, Z.L. Wang, Dissolving behavior and stability of ZnO wires in biofluids: a study on biodegradability and biocompatibility of ZnO nanostructures. Adv. Mater. **18**, 2432–2435 (2006). https://doi.org/10.1002/adma.200600200

15. Q. Wu, X. Chen, P. Zhang, Y. Han, X. Chen, Y. Yan, S. Li, Amino acid-assisted synthesis of ZnO hierarchical architectures and their

novel photocatalytic activities. Cryst. Growth Des. **8**, 3010–3018 (2008). https://doi.org/10.1021/cg800126r

16. P. Basnet, T. Inakhunbi Chanu, D. Samanta, S. Chatterjee, A review on bio-synthesized zinc oxide nanoparticles using plant extracts as reductants and stabilizing agents. J. Photochem. Photobiol. B Biol. **183**, 201–221 (2018). https://doi.org/10.1016/j.jphotobiol.2018.04.036

17. H. Mirzaei, M. Darroudi, Zinc oxide nanoparticles: biological synthesis and biomedical applications. Ceram. Int. **43**, 907–914 (2017). https://doi.org/10.1016/j.ceramint.2016.10.051

18. J. Jiang, J. Pi, J. Cai, The advancing of zinc oxide nanoparticles for biomedical applications. Bioinorg. Chem. Appl. (2018). https://doi.org/10.1155/2018/1062562

19. V.G. Sreevalsa, P.P. Jeeju, M.S. Augustine, K.M. Anilkumar, S. Jayalekshmi, L-Histidine-modified biocompatible zinc oxide nanocrystals. J. Exp. Nanosci. **8**, 937–946 (2013). https://doi.org/10.1080/17458080.2011.624553

20. M. Ramani, S. Ponnusamy, C. Muthamizhchelvan, E. Marsili, Amino acid-mediated synthesis of zinc oxide nanostructures and evaluation of their facet-dependent antimicrobial activity. Colloids Surf. B Biointerfaces **117**, 233–239 (2014). https://doi.org/10.1016/j.colsurfb.2014.02.017

21. B. Liu, H.C. Zeng, Room temperature solution synthesis of monodispersed single-crystalline ZnO nanorods and derived hierarchical nanostructures. Langmuir. **20**, 4196–4204 (2004). https://doi.org/10.1021/la035264o

22. C. Lao, Y. Li, C.P. Wong, Z.L. Wang, Enhancing the electrical and optoelectronic performance of nanobelt devices by molecular surface functionalization. Nano Lett. **7**, 1323–1328 (2007). https://doi.org/10.1021/nl070359m

23. M. Stiboller, G. Raber, K.A. Francesconi, Simultaneous determination of glycine betaine and arsenobetaine in biological samples by HPLC/ICPMS/ESMS and the application to some marine and freshwater fish samples. Microchem. J. **122**, 172–175 (2015). doi:https://doi.org/10.1016/j.microc.2015.04.022

24. R.Y. Gundersen, P. Vaagenes, T. Breivik, F. Fonnum, P.K. Opstad, Glycine—an important neurotransmitter and cytoprotective agent. Acta Anaesthesiol. Scand. **49**, 1108–1116 (2005). https://doi.org/10.1111/j.1399-6576.2005.00786.x

25. E.A. Meulenkamp, Synthesis and growth of ZnO nanoparticles. J. Phys. Chem. B. **102**, 5566–5572 (1998). https://doi.org/10.1021/jp980730h

26. E. Darvishi, D. Kahrizi, E. Arkan, Comparison of different properties of zinc oxide nanoparticles synthesized by the green (using Juglans regia L. leaf extract) and chemical methods. J. Mol. Liq. **286**, 110831 (2019). https://doi.org/10.1016/j.molliq.2019.04.108

27. M.M. Mekonnen, A.Y. Hoekstra, Four billion people facing severe water scarcity. Sci. Adv. **2**, e1500323 (2016). https://doi.org/10.1126/sciadv.1500323

28. M.A. Hanjra, M.E. Qureshi, Global water crisis and future food security in an era of climate change. Food Policy **35**, 365–377 (2010). doi:https://doi.org/10.1016/j.foodpol.2010.05.006

29. S. Sharma, A. Bhattacharya, Drinking water contamination and treatment techniques. Appl. Water Sci. **7**, 1043–1067 (2017). doi:https://doi.org/10.1007/s13201-016-0455-7

30. A. Ajmal, I. Majeed, R.N. Malik, H. Idriss, M.A. Nadeem, Principles and mechanisms of photocatalytic dye degradation on TiO$_2$ based photocatalysts: a comparative overview. RSC Adv. **4**, 37003–37026 (2014). https://doi.org/10.1039/C4RA06658H

31. E.A. Clarke, R. Anliker, Organic dyes and pigments. Handb. Environ. Chem. (1980). https://doi.org/10.1007/978-3-540-38522-6-7

32. D.A. Yaseen, M. Scholz, *Textile dye wastewater characteristics and constituents of synthetic effluents: a critical review* (Springer, Berlin, Heidelberg, 2019). https://doi.org/10.1007/s13762-018-2130-z

33. P.J. Price, W.A. Suk, A.E. Freeman, W.T. Lane, R.L. Peters, M.L. Vernon, R.J. Huebner, In vitro and in vivo indications of the carcinogenicity and toxicity of food dyes. Int. J. Cancer **21**, 361–367 (1978). https://doi.org/10.1002/ijc.2910210318

34. E.Y. Ozmen, S. Erdemir, M. Yilmaz, M. Bahadir, Removal of carcinogenic direct azo dyes from aqueous solutions using calix[n] arene derivatives. Clean Soil Air Water **35**, 612–616 (2007). https://doi.org/10.1002/clen.200700033

35. P. Ribao, J. Corredor, M.J. Rivero, I. Ortiz, Role of reactive oxygen species on the activity of noble metal-doped TiO$_2$ photocatalysts. J. Hazard. Mater. (2019). https://doi.org/10.1016/j.jhazmat.2018.05.026

36. Y. Nosaka, A.Y. Nosaka, Generation and detection of reactive oxygen species in photocatalysis. Chem. Rev. **117**, 11302–11336 (2017). https://doi.org/10.1021/acs.chemrev.7b00161

37. M. Maruthupandy, M. Anand, G. Maduraiveeran, S. Suresh, A.S. Hameedha Beevi, R. Jeeva, Priya, Investigation on the electrical conductivity of ZnO nanoparticles-decorated bacterial nanowires. Adv. Nat. Sci. Nanosci. Nanotechnol. (2016). https://doi.org/10.1088/2043-6262/7/4/045011

38. S. Campisi, M. Schiavoni, C. Chan-Thaw, A. Villa, Untangling the role of the capping agent in nanocatalysis: recent advances and perspectives. Catalysts. **6**, 185 (2016). https://doi.org/10.3390/catal6120185

39. M. Vosoughifar, Influence of capping agents additives on morphology of cadmium tungstate nanoparticles and study of their photocatalytic properties. J. Mater. Sci. Mater. Electron. **28**, 6800–6805 (2017). https://doi.org/10.1007/s10854-017-6377-9

40. E. Emil, G. Alkan, S. Gurmen, R. Rudolf, D. Jenko, B. Friedrich, Tuning the morphology of ZnO nanostructures with the ultrasonic spray pyrolysis process. Metals (Basel) (2018). https://doi.org/10.3390/met8080569

41. C. Dhand, N. Dwivedi, X.J. Loh, A.N. Jie Ying, N.K. Verma, R.W. Beuerman, R. Lakshminarayanan, S. Ramakrishna, Methods and strategies for the synthesis of diverse nanoparticles and their applications: a comprehensive overview. RSC Adv. **5**, 105003–105037 (2015). https://doi.org/10.1039/c5ra19388e

42. D.H. Li, S.F. He, J. Chen, C.Y. Jiang, C. Yang, Solid-state chemical reaction synthesis and characterization of lanthanum tartrate nanocrystallites under ultrasonication spectra. IOP Conf. Ser. Mater. Sci. Eng. (2017). https://doi.org/10.1088/1757-899X/242/1/012023

43. Y. Li, Y. Cao, D. Jia, A general strategy for synthesis of metal nanoparticles by a solid-state redox route under ambient conditions. J. Mater. Chem. A. **2**, 3761–3765 (2014). https://doi.org/10.1039/c3ta14427e

44. H. Yang, J. Yang, Photocatalytic degradation of rhodamine B catalyzed by TiO$_2$ films on a capillary column. RSC Adv. **8**, 11921–11929 (2018). https://doi.org/10.1039/c8ra00471d

45. U. Holzwarth, N. Gibson, The Scherrer equation versus the "Debye–Scherrer equation. Nat. Nanotechnol. **6**, 534 (2011). https://doi.org/10.1038/nnano.2011.145

46. R.F. de Farias, Synthesis and characterization of manganese-glycine and copper-glycine adducts. Quim. Nova **25**, 729–730 (2002). https://doi.org/10.1590/S0100-40422002000500004

47. I. Khan, K. Saeed, I. Khan, Nanoparticles: properties, applications and toxicities. Arab. J. Chem. (2017). https://doi.org/10.1016/j.arabjc.2017.05.011

48. G. Guisbiers, S. Mejía-Rosales, F. Leonard, Deepak, Nanomaterial properties: size and shape dependencies. J. Nanomater. (2012). https://doi.org/10.1155/2012/180976

49. E. Solati, D. Dorranian, Effect of temperature on the characteristics of ZnO nanoparticles produced by laser ablation in water. Bull. Mater. Sci. **39**, 1677–1684 (2016). https://doi.org/10.1007/s12034-016-1315-7

50. M.K. Debanath, S. Karmakar, Study of blueshift of optical band gap in zinc oxide (ZnO) nanoparticles prepared by low-temperature wet chemical method. Mater. Lett. **111**, 116–119 (2013). https://doi.org/10.1016/j.matlet.2013.08.069

51. P.A. Rodnyi, I.V. Khodyuk, Optical and luminescence properties of zinc oxide. Opt. i Spektrosk. (Opt. Spectrosc.) **111**, 776–785 (2011). https://doi.org/10.1134/S0030400X11120216

52. A. Khorsand Zak, R. Razali, W.H. Abd Majid, M. Darroudi, Synthesis and characterization of a narrow size distribution of zinc oxide nanoparticles. Int. J. Nanomed. **6**, 1399–1403 (2011). https://doi.org/10.2147/IJN.S19693

53. T. Academy, R. Academy, S.S. Trakt, 主観的健康感を中心とした在宅高齢者における 健康関連指標に関する共分散構造分析. **3**, 1–21 (1968)

54. V. Srikant, D.R. Clarke, On the optical band gap of zinc oxide. J. Appl. Phys. **83**, 5447–5451 (1998). https://doi.org/10.1063/1.367375

55. J. Wang, Z. Wang, B. Huang, Y. Ma, Y. Liu, X. Qin, X. Zhang, Y. Dai, Oxygen vacancy induced band-gap narrowing and enhanced visible light photocatalytic activity of ZnO. ACS Appl. Mater. Interfaces **4**, 4024–4030 (2012). https://doi.org/10.1021/am300835p

56. D. Pradhan, S.K. Mohapatra, S. Tymen, M. Misra, K.T. Leung, Morphology-controlled ZnO nanomaterials for enhanced photoelectrochemical performance. Mater. Express **1**, 59–67 (2011). https://doi.org/10.1166/mex.2011.1008

57. C. Chen, X. Li, W. Ma, J. Zhao, N. Serpone, Effect of transition metal ions on the TiO_2-assisted photodegradation of dyes under visible irradiation: a probe for the interfacial electron transfer process and reaction mechanism. J. Phys. Chem. B **106**, 318–324 (2002). https://doi.org/10.1021/jp0119025

58. P. Rauwel, M. Salumaa, A. Aasna, A. Galeckas, E. Rauwel, A review of the synthesis and photoluminescence properties of hybrid ZnO and carbon nanomaterials. J. Nanomater. (2016). https://doi.org/10.1155/2016/5320625

59. M. Catauro, E. Tranquillo, G. Dal Poggetto, M. Pasquali, A. Dell'Era, S.V. Ciprioti, Influence of the heat treatment on the particles size and on the crystalline phase of TiO_2 synthesized by the sol–gel method. Materials (Basel) (2018). https://doi.org/10.3390/ma11122364

60. S. Abdul Rashid, S.H. Othman, T.I. Mohd Ghazi, N. Abdullah, Effect of postdeposition heat treatment on the crystallinity, size, and photocatalytic activity of TiO_2 nanoparticles produced via chemical vapour deposition. J. Nanomater (2010). https://doi.org/10.1155/2010/512785

61. K. Bandopadhyay, J. Mitra, Zn interstitials and O vacancies responsible for n-type ZnO: what do the emission spectra reveal? RSC Adv. **5**, 23540–23547 (2015). https://doi.org/10.1039/c5ra00355e

62. S. Steplin Paul Selvin, A. Ganesh Kumar, L. Sarala, R. Rajaram, A. Sathiyan, J. Princy Merlin, I. Sharmila Lydia, Photocatalytic degradation of rhodamine B using zinc oxide activated charcoal polyaniline nanocomposite and its survival assessment using aquatic animal model. ACS Sustain. Chem. Eng. **6**, 258–267 (2018). https://doi.org/10.1021/acssuschemeng.7b02335

63. X. Xing, T. Chen, Y. Li, D. Deng, X. Xiao, Y. Wang, Flash synthesis of Al-doping macro-/nanoporous ZnO from self-sustained decomposition of Zn-based complex for superior gas-sensing application to n-butanol. Sens. Actuators B Chem. **237**, 90–98 (2016). https://doi.org/10.1016/j.snb.2016.06.087

64. H. Wu, M. Qin, A. Chu, Z. Cao, P. Chen, Y. Liu, X. Qu, Effect of urea on the synthesis of Al-doped ZnO nanoparticle and its adsorptive properties for organic pollutants. Mater. Res. Bull. **75**, 78–82 (2016). https://doi.org/10.1016/j.materresbull.2015.11.016

65. C. Karunakaran, V. Rajeswari, P. Gomathisankar, Optical, electrical, photocatalytic, and bactericidal properties of microwave synthesized nanocrystalline Ag–ZnO and ZnO. Solid State Sci. **13**, 923–928 (2011). https://doi.org/10.1016/j.solidstatesciences.2011.02.016

66. H. Kim, H. Jeong, T.K. An, C.E. Park, K. Yong, Hybrid-type quantum-dot cosensitized ZnO nanowire solar cell with enhanced visible-light harvesting. ACS Appl. Mater. Interfaces **5**, 268–275 (2013). https://doi.org/10.1021/am301960h

67. M. Basu, N. Garg, A.K. Ganguli, A type-II semiconductor (ZnO/CuS heterostructure) for visible light photocatalysis. J. Mater. Chem. A. **2**, 7517–7525 (2014). https://doi.org/10.1039/c3ta15446g

68. G.S. Gardner, Handbook of chemistry. J. Franklin Inst. **229**, 138–139 (1940). https://doi.org/10.1016/S0016-0032(40)90947-4

69. Y. Sun, L. Wang, X. Yu, K. Chen, Facile synthesis of flower-like 3D ZnO superstructures via solution route. CrystEngComm **14**, 3199–3204 (2012). https://doi.org/10.1039/c2ce06335b

70. S. Akir, A. Barras, Y. Coffinier, M. Bououdina, R. Boukherroub, A.D. Omrani, Eco-friendly synthesis of ZnO nanoparticles with different morphologies and their visible light photocatalytic performance for the degradation of Rhodamine B. Ceram. Int. **42**, 10259–10265 (2016). https://doi.org/10.1016/j.ceramint.2016.03.153

71. S. Kuriakose, N. Bhardwaj, J. Singh, B. Satpati, S. Mohapatra, Structural, optical and photocatalytic properties of flower-like ZnO nanostructures prepared by a facile wet chemical method. Beilstein J. Nanotechnol. **4**, 763–770 (2013). https://doi.org/10.3762/bjnano.4.87

72. E.R. Nestmann, G.R. Douglas, T.I. Matula, C.E. Grant, D.J. Kowbel, Mutagenic activity of rhodamine dyes and their impurities as detected by mutation induction in Salmonella and DNA damage in Chinese hamster ovary cells. Cancer Res. **39**, 4412–4417 (1979)

73. J.W. Cornick, R.V. Chudyk, L.A. Mcdermott, Toxicity of rhodamine B and fluorescein sodium to fish and their compatibility with antimycin A. J. Progress. Fish-Culturist **0779**, 37–41 (2011). https://doi.org/10.1577/1548-8640(1969)31[139:TORBAF]2.0.CO;2.

74. P. National Toxicology, NTP toxicology and carcinogenesis studies of rhodamine 6G (C.I.Basic Red 1) (CAS No. 989-38-8) in F344/N rats and B6C3F1 mice (feed studies). Natl.Toxicol. Progr. Tech. Rep. Ser. 364, 1–192 (1989). http://www.ncbi.nlm.nih.gov/pubmed/12692640.

75. G. Mishra, M. Mukhopadhyay, TiO_2 decorated functionalized halloysite nanotubes (TiO_2 @HNTs) and photocatalytic PVC membranes synthesis, characterization and its application in water treatment. Sci. Rep. **9**, 1–17 (2019). https://doi.org/10.1038/s41598-019-40775-4

76. D. Samanta, T.I. Chanu, S. Chatterjee, Citrus limetta juice as capping agent in hydrothermal synthesis of ZnS nanosphere for photocatalytic activity. Mater. Res. Bull. **88**, 85–90 (2017). https://doi.org/10.1016/j.materresbull.2016.11.019

77. T.I. Chanu, D. Samanta, A. Tiwari, S. Chatterjee, Effect of reaction parameters on photoluminescence and photocatalytic activity of zinc sulfide nanosphere synthesized by hydrothermal route. Appl. Surf. Sci. **391**, 548–556 (2016). https://doi.org/10.1016/j.apsusc.2016.05.045

78. D. Samanta, T.I. Chanu, P. Basnet, S. Chatterjee, Organic dye degradation under solar irradiation by hydrothermally synthesized ZnS nanospheres. J. Mater. Eng. Perform. **27**, 2673–2678 (2018). https://doi.org/10.1007/s11665-018-3214-0

79. S. Leonardi, Two-dimensional zinc oxide nanostructures for gas sensor applications. Chemosensors **5**, 17 (2017). https://doi.org/10.3390/chemosensors5020017

80. S. Meena, D. Vaya, B.K. Das, Photocatalytic degradation of Malachite Green dye by modified ZnO nanomaterial. Bull. Mater. Sci. **39**, 1735–1743 (2016). https://doi.org/10.1007/s12034-016-1318-4

81. X. Chen, Z. Wu, D. Liu, Z. Gao, Preparation of ZnO photocatalyst for the efficient and rapid photocatalytic degradation of Azo dyes. Nanoscale Res. Lett. **12**, 4–13 (2017). https://doi.org/10.1186/s11671-017-1904-4

82. K. Intarasuwan, P. Amornpitoksuk, S. Suwanboon, P. Graidist, Photocatalytic dye degradation by ZnO nanoparticles prepared from $X_2C_2O_4$(X = H, Na and NH_4) and the cytotoxicity of the treated dye solutions. Sep. Purif. Technol. **177**, 304–312 (2017). https://doi.org/10.1016/j.seppur.2016.12.040

83. S. Bhatia, N. Verma, Photocatalytic activity of ZnO nanoparticles with optimization of defects. Mater. Res. Bull. **95**, 468–476 (2017). https://doi.org/10.1016/j.materresbull.2017.08.019

84. G. Nagaraju, G.C. Shivaraju, G. Banuprakash, D. Rangappa, Photocatalytic activity of ZnO nanoparticles: synthesis via solution combustion method. Mater. Today Proc. **4**, 11700–11705 (2017). https://doi.org/10.1016/j.matpr.2017.09.085

85. M.S. Azmina, R. Md Nor, H.A. Rafaie, N.S.A. Razak, S.F.A. Sani, Z. Osman, Enhanced photocatalytic activity of ZnO nanoparticles grown on porous silica microparticles. Appl. Nanosci. **7**, 885–892 (2017). https://doi.org/10.1007/s13204-017-0626-3

86. U. Alam, A. Khan, D. Ali, D. Bahnemann, M. Muneer, Comparative photocatalytic activity of sol–gel derived rare earth metal (La, Nd, Sm and Dy)-doped ZnO photocatalysts for degradation of dyes. RSC Adv. **8**, 17582–17594 (2018). https://doi.org/10.1039/c8ra01638k

87. D. Neena, K.K. Kondamareddy, H. Bin, D. Lu, P. Kumar, Enhanced visible light photodegradation activity of RhB/MB from aqueous solution using nanosized novel Fe–Cd co-modified ZnO. Sci. Rep. (2018). https://doi.org/10.1038/s41598-018-29025-1

88. R. Ebrahimi, K. Hossienzadeh, A. Maleki, R. Ghanbari, R. Rezaee, M. Safari, B. Shahmoradi, H. Daraei, A. Jafari, K. Yetilmezsoy, S.H. Puttaiah, Effects of doping zinc oxide nanoparticles with transition metals (Ag, Cu, Mn) on photocatalytic degradation of Direct Blue 15 dye under UV and visible light irradiation. J. Environ. Heal. Sci. Eng. **17**, 479–492 (2019). https://doi.org/10.1007/s40201-019-00366-x

89. S.B. Satpal, A.A. Athawale, Synthesis of ZnO and Nd doped ZnO polyscales for removal of rhodamine 6G dye under UV light irradiation. Mater. Res. Express **5**, 085501 (2018). https://doi.org/10.1088/2053-1591/aad26c

90. R. Nagaraja, N. Kottam, C.R. Girija, B.M. Nagabhushana, Photocatalytic degradation of Rhodamine B dye under UV / solar light using ZnO nanopowder synthesized by solution combustion route. Powder Technol. **215–216**, 91–97 (2012). https://doi.org/10.1016/j.powtec.2011.09.014